Cement & Concrete Composites 33 (2011) 925–935

Contents lists available at ScienceDirect

Cement & Concrete Composites

journal homepage: www.elsevier.com/locate/cemconcomp

Discrete modeling of plastic cement paste subjected to drying

V. Slowik [a,*], J.W. Ju [b]

[a] Leipzig University of Applied Sciences, Leipzig, Germany
[b] Department of Civil and Environmental Engineering, University of California, Los Angeles, CA 90095-1593, USA

ARTICLE INFO

Article history:
Received 20 June 2010
Received in revised form 31 January 2011
Accepted 3 February 2011
Available online 26 February 2011

Keywords:
Plastic concrete
Early age cracking
Capillary pressure
Shrinkage
Discrete modeling
Distinct Element Method
Inter-particle forces

ABSTRACT

Prior to initial setting, cement paste may be regarded as a suspension consisting of solid particles and water. Drying leads to a curved water surface in the spaces between the solid particles at the specimen boundary. A negative capillary pressure is built up which results in shrinkage strain and, possibly, cracking. The concept of discrete modeling has been employed for simulating these processes. In 2D models consisting of circular solid particles and a liquid phase, the drying induced capillary pressure build-up and the corresponding particle displacements are simulated by using the Distinct Element Method. Under certain conditions, crack initiation due to capillary forces may be observed. The simulations allow the demonstration of different influences on the risk of plastic shrinkage cracking.

1. Introduction

The present work aims at the modeling of drying induced concrete cracking in the very early age; i.e., within approximately 4 h after casting when the material is still in its plastic stage. In this early age, the hardening process has not yet led to a significant tensile strength of the material. The predominant reason for volume changes and cracking are physical phenomena rather than the beginning chemical reactions. The latter are not decisive for the material behavior in this age, although they do have an influence.

In the following, the material behavior of a drying suspension is described. The corresponding physical processes may be observed in cement paste before initial setting as well as in drying suspensions with inert solid particles. A more detailed description may be found in [1–3].

After the material has been placed in a mold, the solid particles tend to settle due to their self-weight. That is, water is transported to the upper surface. If the water content of the system is high enough, a plane water film is formed on top of the near-surface particles; cf. Fig. 1A. This process is also referred to as bleeding.

Evaporation at an open surface leads to the loss of water from the system. If the solid near-surface particles are no longer covered by a plane water film, the water surface will be curved. In the inter-particle spaces, menisci are formed; cf. Fig. 1B. Accordingly, a capillary pressure is built up in the water phase [1,3–5]. It will be considered as a positive quantity in the following discussion, although the water pressure is lower than that of the surrounding air.

The capillary pressure results in inward forces acting on the particles at the specimen face where evaporation takes place. As a consequence, shrinkage deformations may be observed; i.e., the so-called capillary shrinkage. For cementitious materials, the term plastic shrinkage is also used since this deformation is taking place in the plastic stage.

In the beginning of the capillary pressure build-up, only vertical shrinkage strain may be exhibited; i.e., deformation in the direction perpendicular to the open surface. Subsequently, the material might crack or separate from the side faces of the mold. This allows for horizontal shrinkage strain. The volume change of the drying material is in this stage almost equal to the volume of the evaporating water [1,3,6].

If a certain material specific pressure is reached, not all the inter-particle spaces at the original surface of the drying suspension can be bridged by the menisci anymore. Air penetrates locally into the system, forming weak spots at the surface and allowing crack initiation. It has been shown by scanning electron microscopic observations [1,3,7] and force measurements [3,8] that the local air entry may lead to crack formation in the plastic concrete. However, air entry does not necessarily result in cracks since sufficient particle mobility is also a precondition.

Fig. 2 shows a series of four electron microscopic images taken from the same spot at the surface of a drying suspension made of fly ash and water. In the top image; i.e., at the beginning of the

* Corresponding author. Address: Leipzig University of Applied Sciences, PF 301166, 04251 Leipzig, Germany. Tel.: +49 341 3076 6261; fax: +49 341 3076 7045.
E-mail address: volker.slowik@htwk-leipzig.de (V. Slowik).

0958-9465/$ - see front matter © 2011 Elsevier Ltd. All rights reserved.
doi:10.1016/j.cemconcomp.2011.02.001

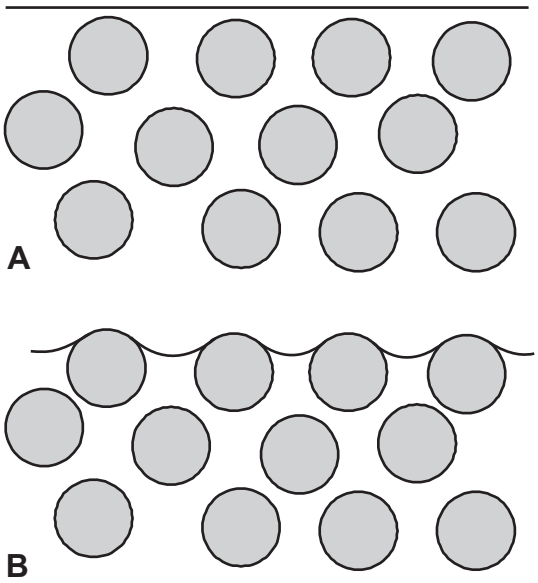

Fig. 1. The surface of a drying suspension. Plane water film covering the solid particles at the surface (A) and formation of menisci in the inter-particle spaces (B).

drying process, all solid particles at the surface are surrounded by water. The contours of these particles are sharper in the second image because the water content of the suspension has been reduced and the particles are sticking out of the water surface. In the third image, dark spots may be seen at the locations where local air entry has taken place. The fourth image shows a crack originating from one of these dark spots demonstrating that air entry may lead to crack initiation. The intention of the presented work was to numerically simulate the complete process illustrated in Fig. 2.

The capillary pressure reached at the first event of air entry is referred to as air entry value. The latter is a material parameter of the suspension and may be identified in laboratory experiments [1,3].

If the capillary pressure in a drying suspension is always lower than the air entry value, cracking is prevented. This is because crack initiation requires air entry. On this basis, a concept of controlled concrete curing in the plastic material stage has been proposed [1,3,7,9]. The capillary pressure build-up in plastic cementitious materials appears to be reversible [3,4]. Hence, it is possible to decrease the capillary pressure by rewetting the surface. Fig. 3 shows the capillary pressure versus time in a cement paste sample. When a predefined threshold of 15 kPa had been reached, the sample was shortly rewetted by dispersing fog above the surface. Only a few seconds of rewetting were required for a significant temporary reduction of the pressure. The rewetting was terminated after the pressure reached a certain lower limit. It is not advisable to reduce the capillary pressure down to zero since, in that case, a plane water film would be created on the surface which might degrade the surface properties of the hardened material. The closed-loop control allows us to keep the capillary pressure within a noncritical range; i.e., between certain predefined limits.

It has been demonstrated that the capillary pressure controlled rewetting of the surface is possible under site conditions and that, in this way, the cracking risk in the plastic stage may be reduced significantly [3,8]. The method requires an in situ capillary pressure measurement which is possible by using wireless sensors [3,9,10]. For rewetting the surface, commercially available fogging devices may be utilized. It must be pointed out that water supply from the concrete surface requires sufficient permeability of the material. This condition is fulfilled in ordinary plastic concrete. However, if the loss of water is predominantly caused by self-desiccation at a later age, rewetting of the surface might be ineffective since the water will not penetrate the material already featuring a reduced permeability. Under such conditions, internal curing might be an appropriate method [11].

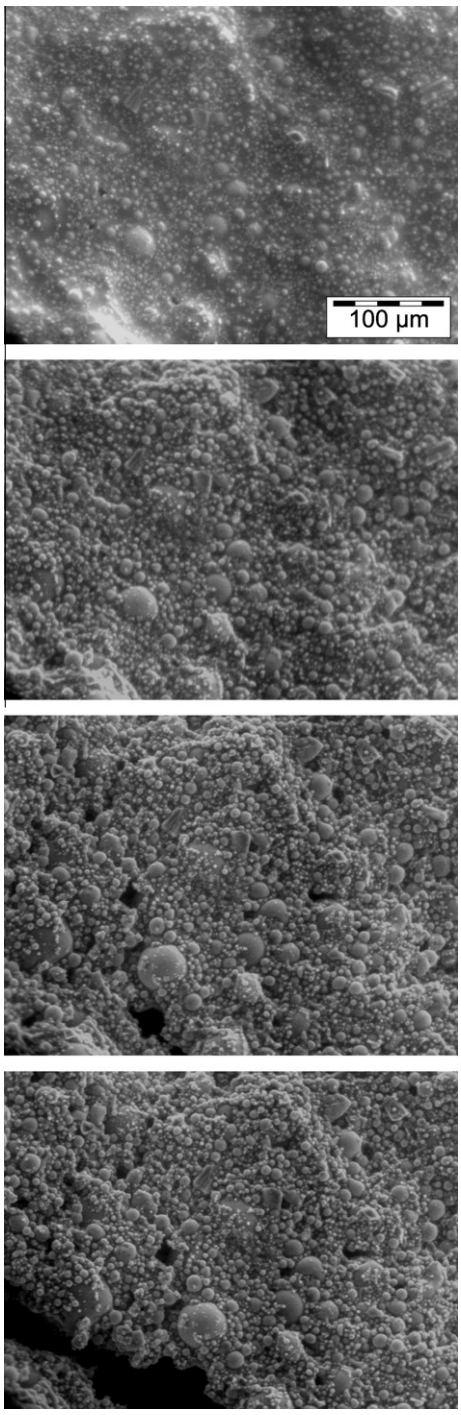

Fig. 2. Electron microscopic images showing the surface of a drying suspension of fly ash and water, at the magnification factor 300, with water content decreasing from top to bottom.

The method of controlled concrete curing requires the identification of a critical capillary pressure which should not be exceeded while the concrete is in its plastic stage. As mentioned before, this threshold should be lower than the material's air entry value. The

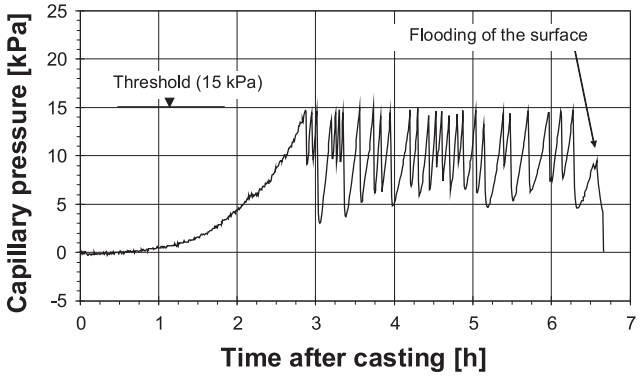

Fig. 3. The capillary pressure versus time during controlled curing of a cement paste sample [7]. The surface of the sample has been rewetted after the threshold value was reached.

latter may be determined experimentally and depends on the surface tension of the liquid, on the particle content and size distribution as well as on the mobility of the particles [3].

In order to obtain a better understanding of the processes leading to air entry and crack initiation, numerical simulations by using Discrete Element Methods are performed. Potentially, the simulation results will also allow us to estimate the critical capillary pressure of a certain material as well as the early age cracking risk. In [2,3], corresponding simulation results were presented and the model assumptions concerning the inter-particle forces were explained. The present paper contains numerical results which are obtained with a different computational solution strategy permitting more extensive and versatile simulations of the underlying problems. Whereas in [2,3] an implicit solution scheme has been adopted, the results presented here were obtained by using an explicit solution scheme which appears to be more efficient from the computational point of view.

2. Outline of the model

2.1. Simulation concept

To simulate the characteristic material behavior of suspensions subjected to drying, the concept of discrete modeling appears to be attractive and appropriate. 2D particle models with circular solid grains are generated. The grains represent cementitious or inert particles of a drying suspension. They are rigid and dispersed in a liquid phase which represents the water. The interaction between the grains is controlled by inter-particle forces. Under the action of external forces, for example of those resulting from capillary pressure or gravitation, the individual solid particles will undergo displacements which may result in global deformations of the specimen or in the formation of cracks.

Particle-based modeling has proved to be a suitable means for simulating the behavior of granular materials. It was applied to fresh cementitious materials for the modeling of particle packing [12,13] as well as for the modeling of microstructural development of cement paste [13]. Recently, particle-based numerical simulations of the drying of suspension droplets in the production process of ceramics were reported [14]. Continuum mechanics based models do not appropriately resemble the granular structure of such materials characterized by changing neighborhood relations between the grains and displacements being larger than the grain sizes.

For the generation of the initial particle structure, a stochastic-heuristic algorithm is adopted here, which was originally developed for concrete meso-level models [15]. The particles are placed in the sample one after the other according to size, starting with the largest one. Firstly, the respective particle is placed at a random position. If it overlaps with previously allocated particles or the specimen boundaries, it is lineally shifted so as to resolve the conflict. If no acceptable position is found after several translational movements, a new random position is generated and tested. This algorithm permits us to obtain considerably higher particle contents than those achieved by a purely stochastic procedure.

Drying of rectangular specimens is simulated [2,3]; see Fig. 4. The top face of the respective specimen is assumed to be open; i.e., evaporation may take place. The other three faces of the specimen are considered to be in contact with the mold. Initially, all particles are completely covered by water. Then, water loss is simulated by incrementally increasing the capillary pressure and calculating the corresponding course of the water front under the assumptions of a wetting angle of zero and a constant curvature according to the respective pressure value. Due to capillary action, this pressure value is inversely proportional to the radii of curvature of the water surface [1–5]. It has a resultant force acting on the particles which are not completely surrounded by the water, i.e., on those at the surface, cf. Fig. 1B, and may lead to particle displacements. After the course of the water front has been calculated, i.e., when the geometry of the specimen surface is known, the total water loss with respect to the initial state may be calculated. In this way, a curve of the capillary pressure versus water loss is obtained. In addition to this curve, the drying simulation yields the pressure dependent particle arrangement on the basis of which shrinkage deformation and crack initiation may be studied.

Despite the limitation of the model to two dimensions, the surface pores are assumed to be axi-symmetric with respect to an axis normal to the surface; i.e., the water menisci are considered to be double-curved forming a spherical surface. Hence, the radius of curvature of the liquid surface is calculated by

$$r = \frac{2\gamma}{p} \tag{1}$$

where r is the radius of curvature; γ the surface tension of the liquid; and p is the absolute value of the capillary pressure.

For the calculation of the total water loss, however, cylindrical menisci in the water front as well as cylindrical solid particles are assumed. The different assumptions concerning the pore shape are made in order to allow a realistic modeling in spite of the two-dimensionality.

Fig. 4 shows the model of a drying suspension under increasing capillary pressure. In the first line, the initial particle arrangement at zero pressure can be observed. All particles (dark circles) are below the water surface. When water (in gray color) evaporates, menisci are formed in the water front between the particles at the surface and, accordingly, a capillary pressure is built up in the liquid phase. This pressure results in downward forces acting on the particles and leading to a settlement of the material. The vertical displacement of the near-surface particles appears to be non-uniform, and air entry into the system does not occur everywhere at the same pressure. It is observed that a local breach is formed at the pressure of approximately 35 kPa. This breach is later widened by the horizontal components of the increasing capillary pressure, and the attracting inter-particle forces decrease to a negligible value. This phenomenon of strain localization and separation is regarded as the crack initiation.

From the results of individual numerical simulations, we can evaluate the curves of the capillary pressure versus water loss as well as the images exhibiting the particle arrangement and the water front under increasing capillary pressure; cf. Fig. 4. The range of capillary pressure values in the simulations is in good agreement with available experimental observations [1,3,7].

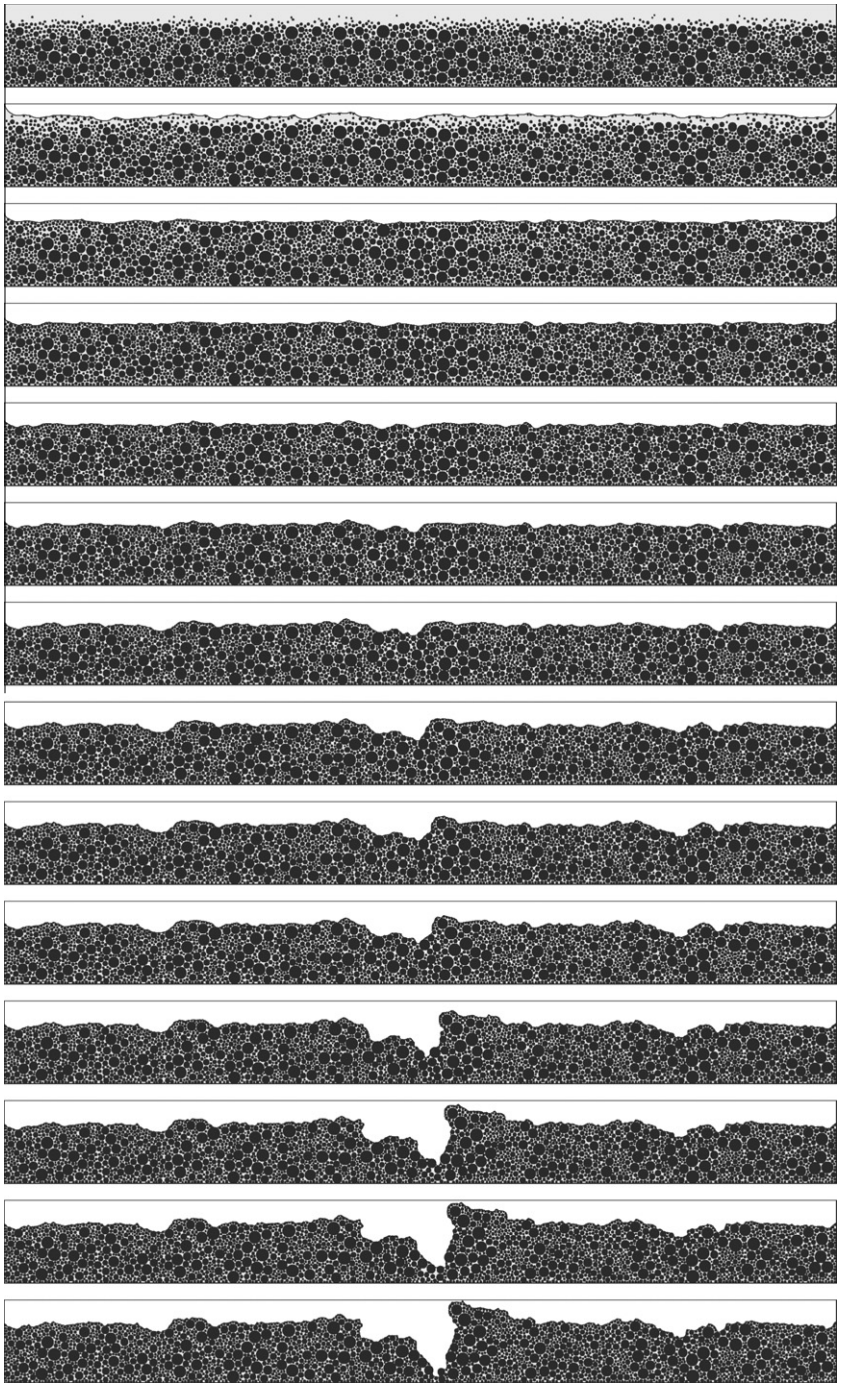

Fig. 4. The simulation of the capillary pressure build-up in a drying suspension. The specimen width is 2 mm, the specimen height is 0.2 mm, and the particle sizes range from 4 μm to 32 μm. The absolute capillary pressure values from top to bottom in kPa are: 0; 4; 10; 15; 20; 25; 30; 35; 40; 45; 50; 54; 55; 56 (approximate values).

2.2. Forces acting on the solid particles

The solid particles are subjected to the following types of forces:

- Gravitational forces.
- Forces resulting from capillary pressure.
- Inter-particle forces.

Gravitational forces are calculated under the assumption of spherical particles. Buoyancy in the liquid phase is taken into account. The capillary pressure results in inward forces acting on those particles which are not completely surrounded by water; see Fig. 5. For the calculation of these resultants, spherical particles are assumed as in the case of gravitational forces.

Between neighboring grains, inter-particle forces are considered; see Fig. 5. They include both the electrostatic F_{el} and the *van-der-Waals* force F_{vdW}. For the *van-der-Waals* force which is always attractive between particles of the same material, a simplified approach according to *Flatt* [16,17] was used:

$$F_{vdW} = A_H \cdot \frac{R}{12 \cdot a^2} \quad \text{with} \quad R = \frac{2 \cdot r_1 \cdot r_2}{r_1 + r_2} \tag{2}$$

where r_1 and r_2 are the particle radii, a is the particle distance, and A_H is the *Hamaker* constant. This force describes the interaction of electrically neutral particles.

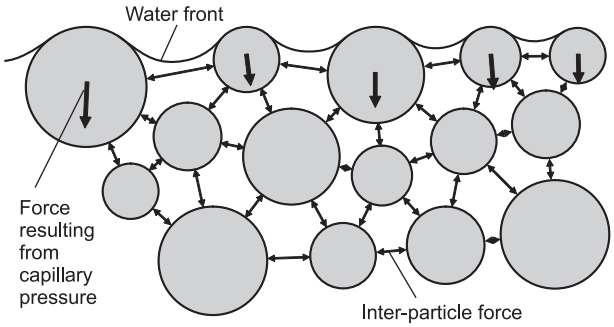

Fig. 5. The forces acting on the solid particles. Gravitational forces are not shown.

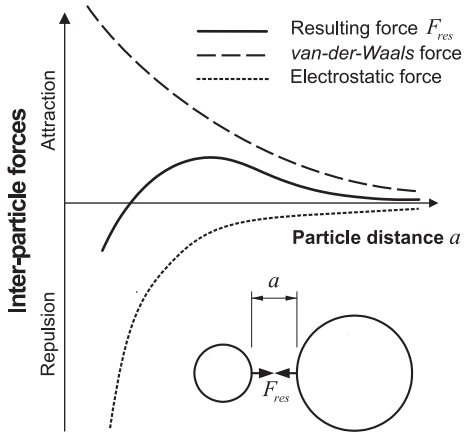

Fig. 6. Inter-particle forces versus particle distance (not to scale).

The electrostatic force results from the repulsion of the ion clouds which are surrounding particles in aqueous solutions. It strongly depends on the properties of the liquid phase. The approach used here was also proposed by *Flatt* [17]:

$$F_{el} = -2 \cdot \pi \cdot \varepsilon_0 \cdot \varepsilon_r \cdot \zeta^2 \cdot R \cdot \frac{1}{\delta} \cdot \frac{e^{-\frac{a}{\delta}}}{1 + e^{-\frac{a}{\delta}}} \quad \text{with}$$

$$\delta = \sqrt{\frac{\varepsilon_0 \cdot \varepsilon_r \cdot k_B \cdot T}{2 \cdot e^2 \cdot z_+^2 \cdot n_+^b}} \tag{3}$$

In Eq. (3), ε_0 is the vacuum permittivity, ε_r the relative permittivity, ζ the zeta-potential, k_B the *Boltzmann* constant, T the absolute temperature, e the elementary charge, z_+ the valence and n_+^b the concentration of an equivalent symmetric electrolyte. The parameter δ is the so-called *Debye* length.

By superposition, a resulting force F_{res} is obtained; see also Fig. 6:

$$F_{res} = F_{vdW} + F_{el} \tag{4}$$

The resulting force is characterized by repulsion in the short-distance range and by attraction at larger particle distances. At the equilibrium particle distance, the value of the resulting force is zero. This distance appears to be particle size independent. The magnitude of the inter-particle forces depends on the properties of the solid particles as well as on the properties of the surrounding liquid. More details of the model assumptions concerning inter-particle forces were given in [2,3].

It should be pointed out that for the inter-particle force in the short-distance and overlapping range, a parabolic function $F_P(a)$ has been adopted which is not directly derived from physical considerations [2,3]:

$$F_P = -f_P \cdot (a - a_{P,S})^2 + F_{P,S} \tag{5}$$

where a is the particle distance; $(a_{P,S}; F_{P,S})$ are the coordinates of the parabola vertex; and f_P is the shape factor. At the transition point, the functions of the original inter-particle force and of the parabola have the same value and the same slope. From these conditions the coordinates of the parabola vertex are derived.

The chosen parabolic function must meet certain requirements of the numerical solution method and may be regarded as a penalty force function which prevents the particle from overlapping and direct contact. In reality, solvation forces [18] and the Born repulsion [19] are acting in the short-distance range. These forces have been included in the aforementioned parabolic function.

Frictional forces are not considered here since the solid particles do not have direct contact. Furthermore, viscosity of the liquid phase is disregarded since the drying induced particle movement is comparably slow. However, the explicit solution method which will be explained later requires the application of damping forces which might be interpreted as an effect of viscosity although they are not derived from the actual physical properties of the liquid.

The physical properties of the solid and liquid phase are kept constant during the simulations. This means that all influences of the cement hydration are disregarded. The modeled material may be considered as a suspension made of inert solid particles and water. Experimental results have shown that in drying suspensions with fly ash the same effects as in plastic cement paste may be observed [1,3].

For the type of material under consideration, the equilibrium particle distance; i.e., the distance at zero inter-particle force in Fig. 6, amounts to a few nanometers. In a 2D model, however, a larger equilibrium particle distance must be assumed. The 2D model represents a section through a 3D specimen. The shortest connecting lines between neighboring particles lie not necessarily within this section. Therefore, the apparent particle distances in the 2D section are larger than in the spatial particle structure. For the simulations presented here, the equilibrium particle distance is adjusted so that the particle content in the unloaded model is in the same order of magnitude as the one in the real material [2,3]. The standard value for the equilibrium particle distance adopted here was 1.5 μm.

2.3. Solution methodology

Previously published simulation results were obtained by using an implicit solution scheme [2,3]. This type of analysis is based on an imaginary truss model, the members of which were the connecting lines between neighboring particles. The latter were considered to be the joints of the truss. External forces resulting from capillary pressure as well as gravitational forces are acting on these imaginary joints. By an iterative matrix stiffness method, a state of equilibrium is searched. In each of the iterations, the connectivity between the particles is updated, i.e., pairs of neighboring particles are identified between which an inter-particle force is acting, and the course of the water front is recalculated. The particle displacements in each iteration depend on the solution of a linear system of equations:

$$\frac{d\Pi(\Delta_1, \ldots, \Delta_i, \ldots, \Delta_n)}{d\Delta_i} = \frac{d(W_{int} - W_{ext})}{d\Delta_i} = 0 \tag{6}$$

where Π is the potential energy of the system; W_{int} and W_{ext} the internal and external work, respectively; Δ_i the displacement at degree of freedom i; and n is the number of degrees of freedom. In this way, the particles are shifted towards directions which minimize the potential energy of the system.

For determining the internal portion of the potential energy, the secant slope of the force–distance curve in Fig. 6 serves as the

"member" stiffness. When previously set convergence limits are reached, the next load step is applied; i.e., the next capillary pressure increment. The convergence criteria are based on particle displacements related to those of the first iteration and on the sum of unbalanced forces related to the maximum "member" force. When the water front is no longer continuous between the side faces of the mold, the simulation is terminated.

In order to reduce the computing time for the simulations, an explicit solution scheme was to be tested as an alternative to the previously described method. Another reason for this is the poor convergence behavior of the implicit solution in the case of larger models. The application of an explicit algorithm was expected to permit a larger particle number in the simulations.

The applied explicit solution scheme is based on the Distinct Element Method (DEM). For consecutive time steps, the acceleration of the particles is calculated:

$$\ddot{\mathbf{u}} = \frac{\mathbf{F}}{m} = \frac{\mathbf{F_e}}{m} + \mathbf{g} \tag{7}$$

where $\mathbf{u}$ is the displacement of the respective particle; $\mathbf{F}$ the sum of forces acting on the particle; $\mathbf{F_e}$ the sum of forces acting on the particle without gravitational force; m the mass of the particle assuming spherical shape; and $\mathbf{g}$ is the gravitational acceleration. Here, forces, displacements and accelerations are all vectors.

On the basis of the acceleration, the velocity and the displacement of the respective particle are calculated by using the central difference method. In order to ensure numerical stability as well as computational efficiency, the length of the time step is adjusted according to the current maximum stiffness:

$$\Delta t = 2\beta \cdot \sqrt{\frac{m_{min}}{k_{max}}}; \quad 0 < \beta \leqslant 1 \tag{8}$$

where Δt is the time step; m_{min} the minimum particle mass in the system; and k_{max} is the maximum contact stiffness in the system. In the simulations presented here, the parameter β was set as 0.1.

Using the comparably small time steps obtained by Eq. (8) on the real time scale which is linked to the actual water evaporation rate would result in a prohibitively high number of required time steps. Therefore, a pseudo-time scale must be adopted for the explicit numerical solution which is separated from the real time scale of the physical process to be simulated. On this pseudo-time scale, the capillary pressure increase is applied at a higher rate, which shortens the computing time for the simulations. In the simulations presented here, this rate was 10^5 kPa s^{-1} (2×10^4 kPa s^{-1} in the simulations for Fig. 13). It has to be considered that the settlement of the solid particles due to their self-weight is also a time dependent process. On the pseudo-time scale it is taking place too slowly, when compared with the capillary pressure build-up. However, for the small particle sizes used here, this discrepancy is not considered to have a significant effect on the simulation results obtained for the consolidated material. Previous simulations with the implicit solution scheme showed that for small particle sizes almost identical results were obtained with and without consideration of the particle's self-weight [20]. The gravitational forces acting on these small particles are negligible when compared with inter-particle and capillary forces.

Forces $\mathbf{F}$ and $\mathbf{F_e}$ in Eq. (7) include a damping force which is required for numerical stability. In the simulations presented here, a mass dependent damping force has been applied:

$$\mathbf{F_d} = -\alpha m \dot{\mathbf{u}} \tag{9}$$

where $\mathbf{F_d}$ is the damping force; m the particle mass; and α is the damping factor. The latter was set to 10^5 s^{-1} for the presented simulations, except for one of those shown in Fig. 8. With this damping factor numerical stability of the solution was ensured. By using an additional stiffness dependent damping force, the performance of the algorithm would not be improved further.

3. Simulation results

3.1. General remarks on the model parameters

In previous parametric studies which were performed by using the implicit solution scheme, some effects of the material composition on the behavior of drying suspensions could be demonstrated [2,3]. The results presented in the following are obtained by using the foregoing explicit solution scheme based on the Distinct Element Method. It is found that with both solution schemes qualitatively the same results are obtained and similar conclusions may be drawn.

For determining the inter-particle forces, generally the same material parameters as in the previous simulations are employed [2,3]. However, for computational reasons, the shape factor f_P determining the opening of the parabola in Eq. (5), which replaces the force–distance curve in the short-distance range, is 10^7 N/m^2 in the simulations presented here; i.e., it is 100 times lower than before. This leads to the parabola branch being less steep, although still significantly steeper than that of the original force–distance curve resulting from electrostatic and *van-der-Waals* forces. With the chosen material parameters [2,3], the parabola branch replaces the actual inter-particle force for distances smaller than the equilibrium particle distance. As stated before, the inter-particle force in the short-distance range is not rigorously derived from physical considerations. It is an artificial penalty force and characterized by a steep increase with reducing particle distance. In the consolidated material stage, this steep increase results in a particle spacing wider than the one arriving from the physically derived force–distance curve. In this treatise, the effect of finer grains not explicitly included in the model but filling the spaces between the actually modeled particles is indirectly taken into account.

If not stated otherwise, a particle area content of 50% was adopted. It relates to the total specimen area including the bleeding film; see Section 3.2.

The scatter of the capillary pressure versus water loss curves obtained in the simulations is remarkably small; i.e., for different random seeds almost identical curves are obtained; see Fig. 7. These curves appear to be material dependent properties. However, they also depend on the specimen height and on the initial particle spacing as will be explained later. Fig. 7 also displays that for different widths of the specimens the same water loss values in

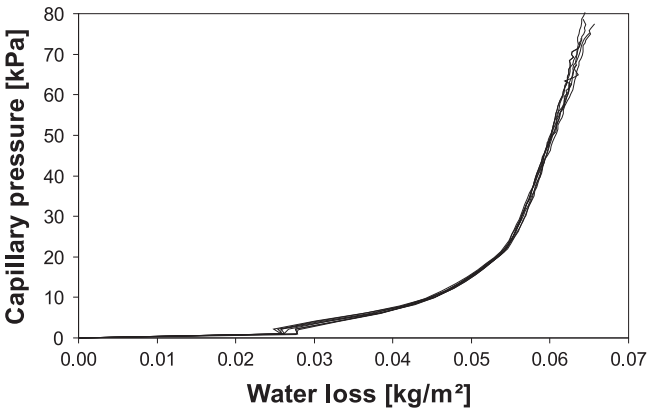

Fig. 7. The capillary pressure versus water loss curves for eight simulations with different random seeds and two different specimen widths; four simulations with width 1 mm and four simulations with width 2 mm. The specimen height is 0.2 mm, and particle sizes range from 4 μm to 32 μm.

kg/m^2 are obtained. It can be concluded that the model dimensions are large enough to yield representative results. In contrast to the pressure–water loss curves, the particle arrangement and the process of crack initiation vary strongly among the individual simulations. Specific conclusions may only be drawn on the basis of repeated simulations with different random seeds.

The curves presented in Fig. 7 have a progressively increasing branch up to a capillary pressure of about 30 kPa and a rather linear branch at higher pressure. Whereas the first branch relates to the consolidation stage, the second branch describes the behavior of the consolidated material, i.e., when the minimum particle spacing for a given external load is reached. This interpretation is based on observations made during the simulations and explained in the following.

For simplicity, the drying suspension may be considered as a one-dimensional vertical series of solid particles and inter-particle spaces. On the upper layer of solid particles, the resultant of the capillary pressure is acting in the downward direction. Between the solid particles, inter-particle forces are present according to the respective particle distance. In addition, damping forces depending on particle mass and velocity are acting. Gravitational forces are also present, but they do not have a significant influence if the solid particles are small; see Section 2.3. If the forces acting on a solid particle are unbalanced, the particle experiences a mass dependent acceleration and a respective inertia force is built up. In this system of particles and inter-particle spaces, the relationship between the capillary pressure and the total water loss depends on both the compliance of the system with respect to the resultant of the capillary pressure and on the capillary pressure value built up due to water loss at the surface. The aforementioned capillary pressure build-up is characteristic for a certain geometry of the surface pores. For the same amount of water disappearing from the surface pores, smaller pore sizes result in a larger curvature of the menisci and, consequently, a higher capillary pressure. The compliance of the system with respect to the resultant of the capillary pressure will depend on the inter-particle forces, on the initial particle spacing, and on the mass of the solid layers, since both inertia and viscous damping are mass dependent. If the model has been consolidated, i.e., if the particle packing is as dense as possible for a given external load, the particle displacements, accelerations and damping forces are small. Hence, the compliance of the system is controlled by the inter-particle force–distance curve; cf. Fig. 6. In the simulations presented in Fig. 7, this is the case above approximately 30 kPa. The steeper the inter-particle force versus distance curve in the short-distance range, the smaller the compliance of the system and the steeper the capillary pressure versus water loss curve will be in the consolidated stage. For a lower pressure, i.e., in the consolidation stage, it can be shown that not only the inter-particle forces have an influence on the course of the capillary pressure versus water loss curve but also the rate of the capillary pressure increase, the damping factor α in Eq. (9), and the initial particle spacing before the capillary pressure is applied. These influences do have an effect on the mobility of the solid particles, on the forces acting on them and, consequently, on the compliance of the system under the action of the increasing capillary pressure. For the consolidated material, however, the capillary pressure versus water loss curve follows a path which is (for a given particle collection) mainly dependent on the formulation of the inter-particle force. The aforementioned other influences vanish. However, if the total particle content varies, the height effect occurs as explained in Section 3.2. Furthermore, smaller particle sizes result in higher capillary pressure and, therefore, a steeper capillary pressure versus water loss curve; see Section 3.3.

The influence of the damping factor α on the capillary pressure versus water loss curve is illustrated in Fig. 8 which shows four curves already presented in Fig. 7. They were obtained for a specimen width of 1 mm by using the explicit solution scheme and the standard value of the damping factor $\alpha = 10^5\ s^{-1}$. The thick curve was obtained with $\alpha = 2 \times 10^5\ s^{-1}$. It may be seen that the damping factor does have an influence in the consolidation stage, but not in the consolidated stage. Higher damping forces impede the movement of the near-surface particles into the water film on the specimen's top face; see last paragraph of Section 3.2. Hence, these particles get in contact with the water front and start to directly resist the capillary forces at higher water loss values. This results in the comparably moderate pressure build-up in the consolidation stage.

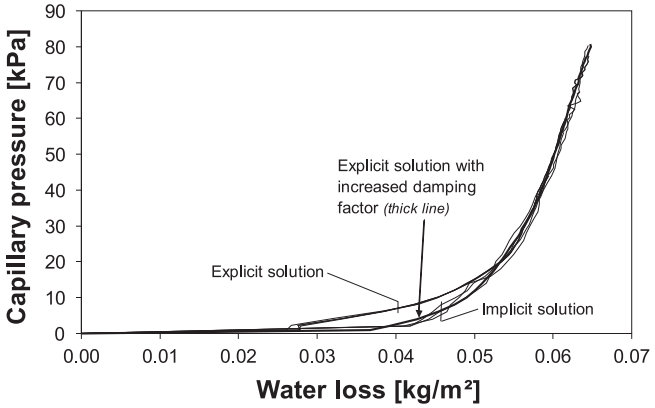

Fig. 8. The capillary pressure versus water loss curves obtained with different solution schemes and parameters, with the specimen width 1 mm, the specimen height 0.2 mm, and particle sizes ranging from 4 μm to 32 μm.

Fig. 8 contains in addition capillary pressure versus water loss curves obtained by using the implicit solution scheme; see Section 2.3. It may be seen that the differences between the two solution schemes are essential only in the consolidation stage. They may be attributed to the different particle mobility in this stage. Once the material is consolidated, the material behavior is almost exclusively controlled by the inter-particle forces and the two solution strategies yield comparable results.

It is concluded that the water loss values obtained in the numerical simulations are strongly dependent on the assumptions concerning the inter-particle forces. In consideration of the simplifications required for the presented simulations, it seems to be inappropriate to exactly match the water loss values measured in experiments. Moreover, the simulation results concerning influences of material parameters on capillary pressure build-up and crack initiation are of much higher interest. Nevertheless, in Section 3.2 an attempt is made to extrapolate the numerically obtained water loss values to heights of laboratory sized specimens.

3.2. Effect of specimen height

It is well known that the water loss values measured under increasing capillary pressure depend on the specimen height [3,5]. This effect may be attributed to the larger compressibility of a higher specimen. As expected, in simulations with different specimen heights, the resulting capillary pressure curves seem to be scaled on the water loss axis; cf. Fig. 9. Table 1 contains the water loss values at a capillary pressure of 40 kPa. These values show linear height dependence as expected. The higher the specimen, the more inter-particle spaces may be compressed under the action of the increasing capillary pressure. In the simulations presented here, a water film on top of the initial particle structure with the standard thickness of 50 μm for a specimen height of 0.2 mm is considered. It represents an initial bleeding film and allows for some movement of the near-surface particles within the

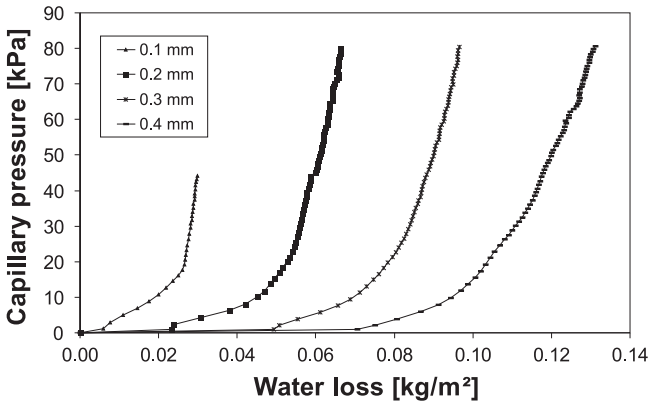

Fig. 9. The capillary pressure versus water loss curves for different specimen heights, with the specimen width 1 mm, the particle content 50%, and particle sizes ranging from 4 μm to 32 μm.

Table 1
Water loss values at a capillary pressure of 40 kPa for different specimen heights, determined on the basis of the curves shown in Fig. 9.

Specimen height (mm)	Thickness of the initial bleeding film (μm)	Total water loss at 40 kPa (kg/m^2)	Total water loss without initial bleeding film at 40 kPa (kg/m^2)
0.1	25	0.0293	0.0043
0.2	50	0.0578	0.0078
0.3	75	0.0870	0.0120
0.4	100	0.1158	0.0158
Linearly extrapolated			
40	0		1.5483
60	0		2.3223
100	0		3.8703

liquid phase prior to the water loss. It has to be pointed out that the value adopted for the film thickness is an assumption. In real experiments, this value would depend on the actual water–solid volume ratio. The bleeding film thicknesses assumed for the different specimen heights are also given in Table 1 and have been considered in the calculation of the water losses specified in the last column. If these data are linearly extrapolated, water loss values in the order of magnitude of experimentally determined values are obtained. Fig. 10 shows measured capillary pressure versus water loss curves for fly ash suspensions [3,20]. In the simulations, the water loss is overestimated by a factor of about two. Considering the simplifications with regard to model size, inter-particle forces and particle size distribution (see Section 3.3), this fidelity confirms the general applicability of the proposed simulation concept. It must also be taken into account that the curves in Fig. 10 show a non-zero slope in the beginning meaning that some consolidation had already taken place before the water loss was recorded. Hence, the total water loss might have been slightly underestimated.

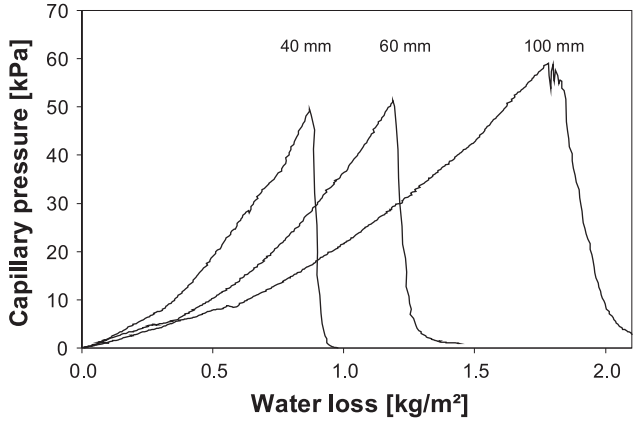

Fig. 10. The experimentally determined capillary pressure versus water loss curves for fly ash samples of different heights [3].

As explained in Section 3.1, in the consolidation phase the initial particle spacing does have an influence on the capillary pressure versus water loss curve. In order to obtain comparable results, the simulations performed with the explicit solution scheme are started in the following fashion. When generating the random particle structure, a minimum distance between the particles and the top face of the specimen is enforced. This distance represents the initial bleeding film thickness. Since the generation algorithm is based on geometrical conditions (avoiding particle overlapping) but not on equilibrium considerations (equilibrium of inter-particle forces acting on the individual grain), the particle positions have to be corrected prior to the actual drying simulation. This is done by applying the Distinct Element Method until convergence criteria based on displacements and unbalanced forces are met. Thereafter, the capillary pressure is incrementally applied. During the preceding position adjustment, the particles are allowed to move into the bleeding film; see particle arrangement for zero pressure in Fig. 4. This phenomenon is regarded as realistic and results in a steady capillary pressure build-up, as it can be observed in experiments [3]. A dense particle packing at the surface leads to an unnaturally abrupt pressure increase.

3.3. Effects of particle size distribution

Three different particle size distributions have been adopted; see Table 2. In the simulations presented so far the particle sizes were ranging from 4 μm to 32 μm. The particle size distribution does have a significant influence on the capillary pressure versus water loss curve. The smaller the minimum particle size, the smaller the surface pores and the higher the curvature of the menisci formed under water loss will be. This generally results in a steeper capillary pressure versus water loss curve, especially in the consolidation phase. Fig. 11 displays curves obtained under different particle size distributions but featuring the same particle content of 50%. The considerably lower water loss values for the particle size distribution 2 ... 32 μm come from the fact that the potential for a further consolidation of the system is limited because of the high total number of solid particles. This characteristic results in a high number of inter-particle spaces with the same equilibrium particle distance as in the case of the other size distributions with fewer particles. In other words, while more and smaller particles are present, the particle spacing is not equally downsized. As a matter of fact, the thickness of the initial bleeding film had to be reduced to 40 μm for the simulations with 2 ... 32 μm in order to fit all the particles into the specimen. For the other two particle size distributions, the total number of particles is significantly lower.

Table 2
Particle size distributions.

Particle sizes (μm)	Area content (%)		
	2 ... 64 μm	2 ... 32 μm	4 ... 32 μm
2 ... 4	11.84	18.24	
4 ... 8	14.29	22.01	26.93
8 ... 16	16.05	24.73	30.24
16 ... 32	22.73	35.02	42.83
32 ... 64	35.09		
Sum	100	100	100

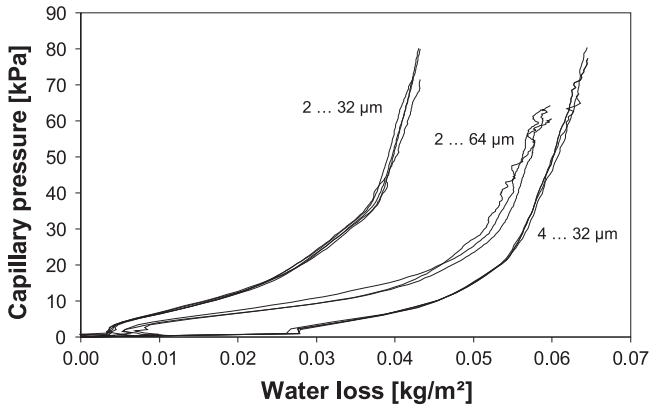

Fig. 11. The capillary pressure versus water loss curves for different particle size distributions, with the specimen width 1 mm, the specimen height 0.2 mm, and the particle content 50%.

The effects of input parameters on the capillary pressure versus water loss curve may be discussed with the help of the simplifying one-dimensional concept outlined in Section 3.1. It would also be possible to use for the actual analyses a one-dimensional approach on the basis of a multi-layer model consisting of permeable solid layers and interlayers representing the inter-particle spaces. The investigation of strain localization and crack initiation, however, requires the usage of a model with at least two dimensions as in the present simulations. Fig. 12 shows exemplarily the particle arrangement under increasing pressure for the different particle size distributions. In most of the simulations, the formation of a "gap" may be observed which is interpreted as air entry or crack initiation. However, no clear trend is found with regard to the influence of the particle sizes on the pressure level at crack initiation, referred to as air entry value in the following. Whereas the scatter of the capillary pressure versus water loss curves is small, the air entry value hardly manifests significant dependency upon the particle sizes, due to its comparably large variance. Possibly, the used specimens are still too small for this task. The simulation results, nevertheless, confirm the observation that plastic concrete is more vulnerable to capillary shrinkage cracking when the minimum particle sizes are small [3]. This may be attributed mainly to the steeper increase of the capillary pressure during the evaporation of water. For a certain water loss, the built up capillary pressure is higher; see Fig. 11.

3.4. Effects of particle spacing

If polyanionic organic polymers are employed as superplasticizers in cementitious materials, then an additional inter-particle force is acting; i.e., the so-called steric force [17]. It arises from polymers being adsorbed at the surface of cement particles and is characterized by a steep increase of the repulsion with decreasing particle distance if the polymeric layers, also referred to as steric layers, of two particles begin to overlap. Approaches for calculating the steric force in cement suspensions were published [17,21]. They reproduce the steep increase of the repulsive force between approaching particles. The steric layer acts like a "wall" hindering further approach. In the present simulations, the short-distance inter-particle force-distance curve is replaced by a parabola with a comparably steep slope; see Section 2.2. This slope may also be considered to act like a "wall" when the particle distance becomes sufficiently small. For this reason, the effect of an additional hindering layer, the steric layer, is simulated by increasing the equilibrium particle distance.

Fig. 13 shows the "crack patterns" obtained in 14 simulations with different random seeds. Seven of these simulations are performed with a 2D equilibrium particle distance of 1.5 µm (particle content 50%) and seven simulations with 3 µm (particle content 40%). These distance values are already up-scaled ones to be employed in the 2D model; cf. Section 2.2. As explained before, it appears to be difficult to identify significant trends concerning a critical capillary pressure from the simulation results. Only on the basis of repeated numerical experiments tendencies may be found. In Fig. 13 the particle arrangements for the larger equilibrium particle distance (right hand side) show a more pronounced formation of "gaps" which might result in cracks. Due to the increased particle mobility in the case of the large equilibrium particle distance, the air entry value (i.e., the pressure at the first event of air entry) seems to be lower than in the case of the small equilibrium particle distance. This observation suggests a higher cracking risk. The same tendency has been found by using the implicit solution scheme [2,3]. It is noted, however, that some of the simulations shown in Fig. 13 do not confirm this tendency.

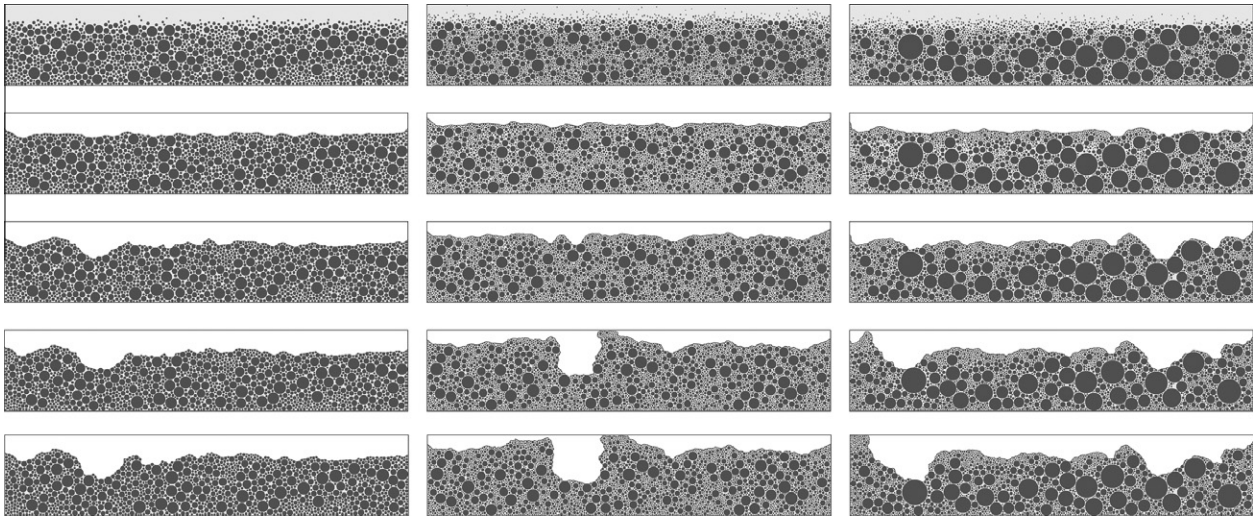

Fig. 12. The simulation of the capillary pressure build-up in drying suspensions, with absolute capillary pressure values from top to bottom in kPa as 0; 20; 35; 45; 50 (approximate values), with particle sizes ranging from 4 µm to 32 µm (left column), from 2 µm to 32 µm (center column), and from 2 µm to 64 µm (right column). The specimen width is 1 mm, the specimen height 0.2 mm, and the particle content 50%.

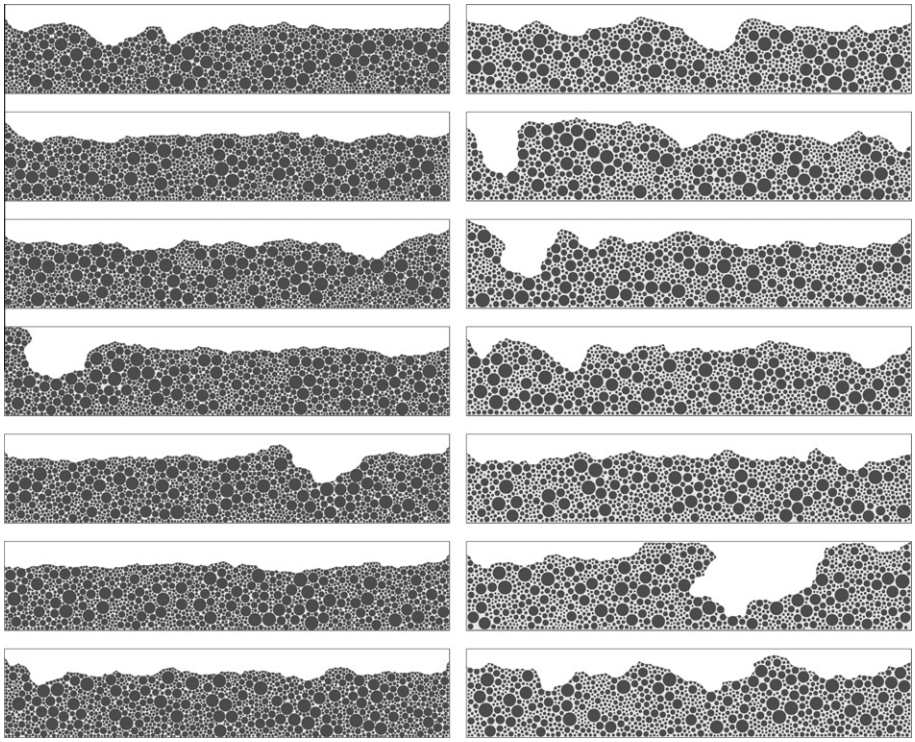

Fig. 13. The particle arrangement in different simulations of the capillary pressure build-up in drying suspensions, for the capillary pressure value 30 kPa (approximate value), particle sizes ranging from 4 μm to 32 μm. The left column involves the equilibrium particle distance 1.5 μm, and particle content 50%. The right column: equilibrium particle distance 3.0 μm, particle content 40%. The specimen width is 1 mm, the specimen height 0.2 mm.

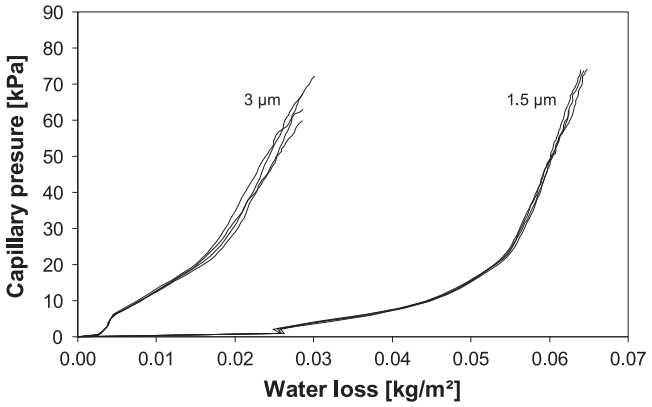

Fig. 14. The capillary pressure versus water loss curves for different equilibrium particle distances, specimen width 2 mm, specimen height 0.2 mm, particle sizes ranging from 4 μm to 32 μm, particle content 50%.

Fig. 14 exhibits curves of the capillary pressure versus water loss for the two different equilibrium particle distances. In order to facilitate a comparison, the particle content is equal to 50% in all these simulations. It may be seen that the material with the smaller equilibrium particle distance shows a higher water loss in the beginning and a stronger consolidation under the increasing capillary pressure. When the material is consolidated, however, the slope of the curve is steeper in the case of the smaller equilibrium particle distance. This may be explained by the smaller surface pores resulting in a higher pressure increase for a certain water loss rate from the surface; see Section 3.1. Despite this steeper increase, a larger equilibrium particle distance is still expected to be accompanied by an increased capillary shrinkage cracking risk. Assuming identical initial porosity, the capillary pressure build-up will start earlier in the material with the larger equilibrium particle distance; i.e., earlier in time for a given water loss rate. In addition, the wider particle spacing results in an increased mobility of the particles and, thereby, promotes strain localization and crack initiation.

4. Concluding remarks

The behavior of drying suspensions has been simulated by using a discrete particle-based model. Effects such as capillary pressure build-up, shrinkage and crack initiation have been demonstrated, and conclusions concerning the cracking risk in plastic cement paste can be drawn.

In general, smaller particle sizes result in a steeper capillary pressure increase which might lead to an increased capillary shrinkage cracking risk. Whereas the curves of the capillary pressure versus water loss show a remarkably small scatter, the obtained particle arrangement and water front images differ strongly and do not permit the identification of significant trends concerning air entry and crack initiation. However, a slight tendency towards an increased cracking risk with increasing equilibrium particle distance is found.

Whereas for previously published results [2,3] an implicit solution scheme was applied, the results presented here were obtained by using the Distinct Element Method as an explicit solution scheme. The findings of the previous simulation work could be confirmed.

It should be indicated that the model does not yet include age-dependent material properties and the evolution of the particle sizes due to cement hydration. However, plastic cement paste and suspensions with inert solids show a similar drying behavior.

Acknowledgment

The work of the first author was performed under a Fulbright Scholarship. This support is gratefully acknowledged.

References

[1] Slowik V, Schmidt M, Fritzsch R. Capillary pressure in fresh cement-based materials and identification of the air entry value. Cem Concr Compos 2008;30(7):557–65.

[2] Slowik V, Hübner T, Schmidt M, Villmann B. Simulation of capillary shrinkage cracking in cement-like materials. Cem Concr Compos 2009;31(7):461–9.

[3] Slowik V, Schmidt M. Kapillare Schwindrissbildung in Beton (Capillary shrinkage cracking in concrete). Berlin: Bauwerk Verlag GmbH; 2010.

[4] Wittmann FH. On the action of capillary pressure in fresh concrete. Cem Concr Res 1976;6:49–56.

[5] Radocea A. A study on the mechanism of plastic shrinkage of cement-based materials. PhD thesis, Göteborg, Chalmers University of Technology, Göteborg; 1992.

[6] Grube H. Definiton der verschiedenen Schwindarten, Ursachen, Größe der Verformungen und baupraktische Bedeutung. Beton 2003;12:598–603.

[7] Schmidt D, Slowik V, Schmidt M, Fritzsch R. Auf Kapillardruckmessung basierende Nachbehandlung von Betonflächen im plastischen Materialzustand (Early age concrete curing based on capillary pressure measurement). Beton Stahlbetonbau 2007;102(11):789–96.

[8] Slowik V, Schmidt M, Neumann A, Dorow J. Early age cracking and its influence on the durability of concrete structures. In: Tanabe T, Sakata K, Mihashi H, Sato R, Maekawa K, Nakamura H, editors. Proceedings of the 8th international conference on creep, shrinkage and durability mechanics of concrete and concrete structures (CONCREEP 8), September 30–October 2, 2008, vol. 1. Ise-Shima, Japan. London: Taylor & Francis Group; 2008. p. 471–7.

[9] Slowik V, Schmidt M, Villmann B. Capillary shrinkage cracking – Experiments and numerical simulation. In: Oh BH, Choi OC, Chung L, editors. Fracture mechanics of concrete and concrete structures. Proceedings of the 7th international conference on fracture mechanics of concrete and concrete structures (FraMCoS-7), May 23-28, 2010, vol. 2. Jeju, Korea. p. 739–44.

[10] Schmidt M, Slowik V. Capillary shrinkage cracking and its prevention by controlled concrete curing. In: Kovler K, editor. Proceedings of the 2nd international RILEM workshop on concrete durability and service life planning (ConcreteLife'09), September 7–9, 2009, Haifa, Israel. Bagneux, France: RILEM Publications S.A.R.L. p. 23–30.

[11] Henkensiefken R, Bentz D, Nantung T, Weiss J. Volume change and cracking in internally cured mixtures made with saturated lightweight aggregate under sealed and unsealed conditions. Cem Concr Compos 2009;31(7):427–37.

[12] He H. Computational modelling of particle packing in concrete. PhD thesis. Delft University of Technology, The Netherlands; 2010.

[13] Stroeven M. Discrete numerical modelling of composite materials. PhD thesis. Delft University of Technology, The Netherlands; 1999.

[14] Nishiura D, Shimosaka A, Shirakawa Y, Hidaka J. Simulation of drying of particulate suspensions in spray-drying granulation process. J Chem Eng Japan 2010;43(8):641–9.

[15] Leite JPB, Slowik V, Apel J. Computational model of mesoscopic structure of concrete for simulation of fracture processes. Comput Struct 2007;85(17–18):1293–303.

[16] Flatt RJ. Dispersion forces in cement suspensions. Cem Concr Res 2004;34(3):399–408.

[17] Flatt RJ. Towards a prediction of superplasticized concrete rheology. Mater Struct 2004;37(269):289–300.

[18] Churaev NV, Derjaguin BV. Inclusion of structural forces in the theory of stability of colloids and films. J Colloid Interf Sci 1985;103(2):542–53.

[19] Feke DL, Prabhu ND, Mann Jr JA, Mann JA. A formulation of the short range repulsion between spherical colloidal particles. J Phys Chem 1984;88(23):5735–9.

[20] Hübner T. Zur Simulation der kapillaren Schwindrissbildung in aus-trocknenden Suspensionen. MSc thesis. Leipzig, Germany, Leipzig University of Applied Sciences; 2007.

[21] Kjeldsen AM, Geiker M. Modelling inter-particle forces and resulting agglomerate sizes in cement-based materials. In: Proceedings of SCC2005 – combining the second North American conference on the design and the use of self-consolidating concrete and the fourth international RILEM symposium on self-compacting concrete, October 30–November 2, 2005, Chicago, Illinois, USA. p. 105–13.